https://doi.org/10.1016/j.msea.2018.11.148

A novel ferritic steel family hardened by intermetallic compound G-phase

Mujin Yang[a], Jiahua Zhu[a], Tao Yang[b], Junhua Luan[b], Zengbao Jiao[c], Xiuru Fan[d], Bernd Kuhnd, Xiangyuan Xiong[e], Cuiping Wang[a,*], Chain Tsuan Liu[b], Xingjun Liu[a,f,**]

[a] *College of Materials and Fujian Provincial Key Laboratory of Materials Genome, Xiamen University, Xiamen 361005, China*

[b] *Department of Mechanical and Biomedical Engineering, City University of Hong Kong, Hong Kong, China*

[c] *Department of Mechanical Engineering, The Hong Kong Polytechnic University, Hong Kong, China*

[d] *Forschungszentrum Jülich GmbH, Institute for Energy and Climate Research, Microstructure and Properties of Materials (IEK-2), 52425 Jülich, Germany*

[e] *College of Materials Science and Engineering, Beijing University of Technology, Beijing 100124, China*

[f] *Department of Materials Science and Engineering, Harbin Institute of Technology, Shenzhen, Guangdong 518055, China*

ABSTRACT

In this paper, G-phase precipitation and the resulting hardening effect on Fe-20Cr-3Ni-1Mn-3Si ferritic alloys by the addition of Ti, Nb, Ta and Zr were individually studied by electron microscopy and atom probe tomography, combined with thermodynamic and first principle calculations. The high resolution scanning electron and transmission electron microscopy observations confirmed that four kinds of $Ni_{16}M_6Si_7$ (M=Ti, Nb, Ta and Zr) Gphase particles were distributed uniformly in the matrix of the four alloys aged at 560–860 °C. The 3D-APT results revealed the formation of the four different nanoscale precipitates, with the highest number density (6.05×10^{23} m^{-3}) and smallest radius (1.64 ± 0.45 nm) in the Ti added alloy. The nanoscale sized precipitates stability (~3 nm for Ti added alloy; ~5 nm for Nb added alloy and Zr added alloy; ~25 nm for Ta added alloy) was attributed to their particular

cube-cube orientation relationships, which led to a very low interfacial energy. The effects of the G-phase on precipitation hardening and quasi steady-state deformation resistance were examined. The 560 °C-aging hardening experiments suggested a rapid precipitation process of the nano-particles. The peak hardness values of the four alloys are in the descending order: Ti >> Nb>Ta >> Zr. The 660 °C quasi steady-state deformation experiments showed threshold stresses of 110 and 140 MPa in cases of the Nb and Ti added alloys, which were higher than that of the previously reported B2-NiAl strengthened steels and commercial heat-resistant steels. By using the formation of nanoscale G-phase precipitates, a new ferritic steel family with very high strength and creep resistance has been proposed. Further alloy optimization is in progress.

Keywords: Nano-precipitates High-performance steels G-phase Atom probe tomography

1. Introduction

To improve high strength steels for service at high temperature, several high performance materials strengthened by nano-scale precipitates, like MC-carbides [1,2], B2-NiAl [3–6], Ni3Ti [7], Cu-rich phase [8] and κ-carbides [9,10], have been developed. These nanoprecipitates have become more and more important microstructural constituents in the development of high strength and creep resistant steels. It is known that the MC-carbides could be introduced into lowalloy steels to achieve high strength [1,2] through alloying strong carbides forming elements, such as Ti, V, Mo and Nb. These MC-carbides nucleate preferentially at austenite/ferrite interfaces and typically show a periodic distribution structure of nano-scale lines [11], introducing a precipitation hardening effect. Similarly, the hierarchically structured NiAl/Ni2TiAl precipitates

developing in alloys based on FBB8 (Fe-10Cr-10Ni-6Al-3.4Mo-0.25Zr-0.002B) lead to high creep resistance at 700 °C [3–6,12–17]. More recently, it was reported that high-density, fully coherent B2-NiAl nano-precipitates with low lattice misfit and high anti-phase boundary energy were developed in maraging steels to strengthen the alloy up to 2.2 GPa without sacrificing ductility [18], demonstrating a significant impact of nano-precipitates in combing high strength and high ductility in steels. In contrast to the periodic distribution of nano-precipitates, a random distribution of Curich precipitates is reported to form in precipitation hardening (PH) steels, when Cu is added. The crystal structure evolution sequence of the Cu-rich precipitates is body centred cubic (bcc) → 9R → face centred cubic (fcc) [8,19–22]. In lightweight Fe-Mn-Al-C steels, nanosized κ-carbides of L′12 ordered structure are found to be responsible for homogeneous shear band formation accompanied by planar slip, resulting in shear band induced plasticity (SIP) [9,10,23].

Another type of precipitate that has strong impact on the mechanical properties of ferritic and austenitic steels is the G-phase. Although some early works on reactor pressure vessels (RPVs) steels claimed that the G-phase was a preferable nucleation site of microcracks by particle cracking [24,25], our recent work found that the G-phase could serve effectively in dispersion strengthening of ferritic steels [26,27].

To develop high performance, low cost ferritic steels, it is important to find proper precipitates as dispersion strengthening phase and an effective way to introduce this phase into the alloy and to modify the microstructure of the alloy. This paper presents a systematic study on the microstructures and mechanical properties of four alloys (Fe-20Cr- 3Ni-1Mn-3Si-2X, where X=Ti, Nb, Ta and Zr in wt%) applying high resolution scanning electron, transmission electron microscopy and atom probe tomography, with the aim to develop the technological basis for a novel ferritic steel

family strengthened by nano-sized Gphase precipitates. Applying thermodynamic and first principle calculations, the selection of alloying elements and the resulting precipitate microstructure of the G-phase as well as their effects on the precipitation hardening effect have been discussed.

2. Experimental procedure

Four alloy ingots of the nominal compositions shown in Table 1 were prepared combined arc- and induction-melting technology using commercially-pure metals (99.99% in purity, supplied by the Institute of Ferrous Metallurgy (IEHK), Northrhine Westfalian Technical University (RWHT), Aachen) at the Peter Grünberg Institute (PGI-5) at Forschungszentrum Jülich, Germany. The alloying elements (Ti, Nb, Ta and Zr) were added in an amount of 2 wt%, which may be considered excessive. The reason for this "over-alloying" will be explained in the following (cf. Section 4.1). The cast ingots were then homogenized at 1200 °C for 30 min in evacuated quartz capsules, quenched in ice water and then cut into small pieces for the aging heat treatment in the temperature range from 560° to 860°C for various times ranging from 0.25 to 96 h in air, followed by air-cooling on a ceramic block.

Compression deformation specimens with a dimension of 3mm in diameter and 3.5mm in height were fabricated from the ingots by electric discharge machining (EDM). An MTSE45.504 closed-loop testing machine equipped with an all ceramic loading apparatus and a 5 kN load cell was utilized for the high temperature compression deformation tests, described in the literature [28], performed at 660 °C.

Scanning electron microscopy (SEM) specimens were cut from aged samples, cold mounted with epoxy resin and polished to a sub-micron finish applying a suspended diamond polishing solution. The microstructural evolution was examined by

high-resolution field emission scanning electron microscopy (HR-FESEM) (backscatter or secondary electron imaging). The phase compositions were analyzed utilizing a Zeiss Merlin SEM with energy dispersive x-ray detector (EDX). The SEM specimens were also utilized in micro-hardness testing applying a Shimadzu Micro-Hardness Tester (4.9 N Load and 15 s holding time) to evaluate the age-hardening phenomenon. Each sample was tested seven times and average values of the measured data were taken.

Transmission electron microscopy (TEM) specimens were initially ground to a thickness of ~50 μm and then electro-polished in an electrolyte of 6% HClO4, 12% CH3COOH and 12% ethylene glycol in methanol at 28 V at room temperature. Thin foils were examined in a JEM- 2100 (HC) TEM operating at 200 kV. The images were analyzed by applying the open source software package Image J.

Needle-shaped atom probe tomography (APT) specimens were fabricated by annular milling in a FEI Scios focused ion beam/scanning electron microscope (FIB/SEM) [26]. APT characterizations were performed in a local electrode atom probe (CAMECA Instruments LEAP 5000X HR). The specimen was analyzed in voltage mode, with a specimen temperature of 50 K, a pulse repetition rate of 200 kHz, a pulse fraction of 0.2 and an ion collection rate of between 0.5% and 1% ions per field evaporation pulse. Interactive Visualization and Analysis Software (IVAS, Version 3.8) was utilized for three-dimensional reconstructions, composition analyses and the creation of isoconcentration surfaces.

Thermo-Calc 3.0.1 with the Fe-based database (TCFE7) was used for thermodynamic equilibrium calculations. For simplicity, only four kinds of phases (G-phase, Laves phase, ferrite and austenite) were selected while other minor other phases (like carbide) were ignored. Firstprinciple calculations were used to calculate

the formation entropy of the G-phase structure based on the density functional theory implemented in the Vienna ab-initio Simulation Package [27]. Projectoraugmented wave potential and the Perdew–Burke–Ernzerhof generalized gradient approximation were used to describe the Coulomb interaction of ion cores with the valence electrons and the electronic exchange, respectively [28]. Brillouin zone sampling was performed using the Monkhorst-Pack scheme [18] with a 6×6×6 k-mesh. Throughout the calculation, the convergence of the total energy and the maximum force of ionic relaxation were set to less than 10−5 eV/atom and 10−2 eV/Å, respectively.

3. Results

3.1. Mechanical properties

The mechanical properties of the alloys were examined through micro-hardness and compression deformation tests as shown in Fig. 1a and b, respectively. Isothermal ageing was carried out at 560 °C for different time from 0.25 to 96 h after solution treatment at 1200 °C for 30 min. All solution-treated specimens showed a relatively low microhardness (Fig. 1a), in the range from 260 to 300 HV. The hardness differences in the initial state could be attributed to the solution strengthening effects of different alloying elements. The peak-hardness occurred between 8 and 10 h except for the XD-Ta alloy, in which it occurred at ~24 h due to the slowest diffusion rate among the four alloying elements. In addition, the values of peak-hardness were different for the four alloys. The highest peak hardness occurred in case of the XD-Ti alloy, reaching up to ~620 HV. The peak hardnesses of the XD-Nb and XD-Ta alloys were much lower, about ~410 and ~390 HV. The XD-Zr ingot reached the lowest peak hardness of ~310 HV. After further aging treatment, the hardness decreased slightly, indicating that G-phase particles experienced a slight coarsening process. It should be noted that the

observed quick precipitation in our case was different from other reports on G-phase [29–31], according to which it was a harmful phase that occurred after a long-term aging of up to tens of thousands of hours.

Fig. 1b displays the quasi steady-state deformation rate as a function of applied stress at 660 °C for the XD-Ti and XD-Nb alloys. The data for FBB8 and other creep resistant steels from Refs. [32,33] were plotted for comparison. At low stresses (points marked by downward arrows in Fig. 1b), a quasi-steady-state deformation rate was not achieved. Several trend lines were introduced to Fig. 1b referring to the effect of two kinds of G-phase on the deformation properties. In comparison to the XD-Nb alloy, the quasi steady-state deformation rate of the XD-Ti alloy was found to be significantly reduced by about two orders of magnitude at corresponding stresses (Fig. 1b). Furthermore, the slopes of the linear fits of the strain-rate vs. stress data depicted in double logarithmic plots in Fig. 1b correspond to apparent stress exponents (n_{app}=27 for XD-Nb and 21 for XD-Ti at high applied stresses), which were found to be much higher than that of a single phase Fe-24Cr-4Al alloy solid solution under similar conditions [34]. High stress exponents usually imply strong interaction between the precipitates and matrix dislocations, which could be expressed by a threshold stress [35]. The strain rate can be expressed using the modified Mukherjee-Bird-Dorn equation in precipitate-strengthened alloys:

$$\dot{\varepsilon} = A\left(\frac{\sigma_a - \sigma_{th}}{\mu}\right)\exp\left(\frac{-Q}{k_B T}\right) \quad (1)$$

where A is a constant, μ is the shear modulus of the matrix, σ_a is the applied stress, σ_{th} is threshold stress, n is the matrix stress exponent and Q is the creep activation energy, k_B is Boltzmann's constant and T is temperature. A value of n=4 was applied for the matrix stress exponent like in the Fe-Ni-Al-Cr alloys reported in [36]. The threshold stress at strain rates above 1×10^{-8} s^{-1}, estimated by a linear leastsquares regression of

$\varepsilon^{1/n}$ vs. $\sigma a - \sigma th$ with n=4, were ~140 MPa for XD-Ti and ~116 MPa for XD-Nb, both of them higher than that of the FBB8 steel (~112 MPa) [36]. All these results suggest that G-phase hardened steels might provide better technological basis for the development of highly heat resistant steels for application beyond 620 °C than B2-NiAl strengthened FBB8 or commercial ferritic-martensitic steels.

3.2. Microstructural investigation

The microstructural features of the four alloys were investigated by SEM, as shown in Fig. 2. The grain sizes and grain boundary structures differ in the 560 °C / 8 h aging specimens. A simplest single phase microstructure was observed in the XD-Ti alloy. No precipitate phase was detected in the grain interiors or at the grain boundaries (cf. Fig. 2a, b and c). Fig. 2d to f present the microstructures of the XD-Ta alloy. Spherical particles of small size (~20 nm) appear at the grain boundaries while the grain interior seemed to be completely free of precipitates. Similar microstructures were observed in case of the XD-Nb and XD-Zr alloys. The grain sizes of these two alloys are much smaller than those of the XD-Ti and XD-Ta alloys (cf. Fig. 2g and j) and some comparably large primary particles occur in the grain interiors. The grain refinement effect may be attributed to the presence of grain boundary precipitates. The primary particles were identified as Laves phase by EDS analysis (cf. Table 2), which may be Nb-rich Fe_2Nb and Zr-rich Fe_2Zr (Fig. 2h and k). Fig. 2i and l present grain boundary microstructures taken at a higher magnification of ×50 k. Fig. 2(i, the aged XD-Nb alloy) clearly depicts few secondary phase particles located at the grain boundaries. In the XD-Zr alloy obviously two different contrasts are located at the grain boundaries (cf. Fig. 2l). They were very probably two kinds of Zr-rich Laves phases (white-C15 and grey- C36 types).

3.3. High-resolution SEM microstructure

To identify nano-sized G-phase precipitates in the four alloys, totally 16 peak-aged specimens (at 560 °C, 660 °C, 760 °C and 860 °C) of the four studied alloys were examined by high-resolution SEM. However, only the XD-Ta specimens showed G-phase precipitates (cf. Fig. 3). Fig. 3a, b and c present high-resolution micrographs, taken from the 660 °C / 15 min, 760 °C / 15 min, 860 °C / 15 min aging XD-Ta specimens. Distinction between G- and Laves-phase particles by size only is sluggish, because the fine G-phase and slightly bigger Laves phase particles appear randomly distributed in both the matrix and at the grain boundaries. It should be noted that grain boundary coverage does not necessarily mean embrittlement in numerous materials reported in literature [37–40]. The G-phase precipitates in the other three alloys were too small to be analyzed by SEM, but could be observed by TEM analysis (cf. Section 3.3).

3.4. TEM observations

Four dark field images (Fig. 4a, c, f and i) and its corresponding electron diffraction patterns (Fig. 4b, d, g and j) demonstrated four kinds of G-phase nano-particle types in the four alloys. The TEM specimens were cut from the 560 °C / 8 h aged XD-Ti, 660 °C / 8 h aged XDNb / Zr and 760 °C / 8 h aged XD-Ta. Comparing the four over-aged microstructures (Fig. 2), the differences in particle sizes are clearly observable. Statistical analysis (Fig. 4e, h, k) yielded that the Nb-/Zrtype G-phase particle size (~6 nm / ~5 nm) was roughly equal and close to the SEM resolution limit. The Ta-type G-phase particles (~25 nm) were the largest. The smallest particles were the Ti-type Gphase precipitates. Large angle tilting was applied for acquiring the comparatively weak patterns from the very small G-phase particles (cf. Fig. 4b). It

should be noted that the particular cubic-cubic orientation relationships between the matrix and precipitate causes low interfacial energy, and thus may effectively prevent particles from coarsening [26,27,30,41]. The precipitates in the XD-Ti specimen were further analyzed by APT (cf. Section 3.4).

3.5. APT analysis

APT was applied to characterize the Ti-type G-phase, which was the smallest one among the four alloys. APT reconstruction maps are presented in Fig. 5a for illustrating the partitioning of elemental species to the precipitates. As expected for the Ti-type G-phase, precipitates were enriched in Ni, Ti and Si together with a small amount of Fe, Cr and Mn, which was highly consistent with the corresponding atom maps (cf. Fig. 5c). Fig. 5b presents the 10 at% Ni-isoconcentration surface illustrating the ultrafine spherical precipitates. Statistical analyses revealed that the aged XD-Ti alloy contained approximately equiaxed particles with radii of 1.6 ± 0.5 nm and a number density of 6.1×10^{23} $m^{-3.}$ As the size of partial particles cannot be calculated, the average radius may be under-estimated. The high particle-number-density is consistent with the measured high level micro-hardness and low high temperature deformation (Fig. 1). The Ni-, Ti- and Si- atomic maps (high resolution) presented in Fig. 5c represent the particle marked by a red circle in Fig. 5b. A proximity histogram constructed on the basis of the 10 at% Ni isoconcentration surface is shown in Fig. 5d. Fe and Cr predominantly partition to the matrix, whereas Ni, Ti and Si do partition mainly to the precipitates. In contrast, Mn seems to not preferentially partition to either the matrix or the precipitates. The chemical compositions of the precipitates and matrix were estimated from APT data (cf. Table 3). The atomic ratio of Ni: Ti: Si in the nanoparticles is non-stoichiometric, and the average composition can be assumed to be

37.7Ni–17.6Fe–16.0- Ti–23.0Si–5.6Cr (at%). Previous studies [42] found that Fe can occupy the sublattice of Ni in the $Ni_{16}Ti_6Si_7$ phase, whereas Cr can occupy the sublattice of Ti. Therefore, the composition of the G-phase in the XD-Ti alloy can be estimated to be $(Ni,Fe,Cr)_{16}(Ti,Cr)_6Si_7$.

4. Discussion

The four trial alloys presented not only submicron precipitates (Laves phase) located at grain boundaries, but also a high number density of nano-sized particles (G-phase) in the grain interiors. These precipitates effectively hinder dislocation movement and thus grain growth and deformation. For this reason the presented trial alloys can be considered strong and creep-resistant.

4.1. G-phase in the ternary phase diagram

The G-phase is a ternary silicide with a chemistry formula of $A_{16}M_6Si_7$ (A=Fe, Ni, Co; M=transition elements). All the known ternary G-phases were collected, classified and presented in Table 4. Except three metastable G-phases ($Fe_{16}Nb_6Si_7$/$Fe_{16}Ta_6Si_7$/$Ni_{16}Cr_6Si_7$), totally fifteen ternary G-phases have been experimentally determined in previous research. It could be found that Group IV (Ti, Zr, Hf) and group V (V, Nb, Ta) elements were strong G-phase forming agents. For Group VI and VII, only two ternary G-phases (metastable Ni16Cr6Si7 and stable $Ni_{16}Mn_6Si_7$) were certain. This was a main reason for the alloy design presented (Ti-, Nb-, Zr-, Hf- and Ta-alloying) in this paper. And the “over alloying” strategy (2 wt% addition amount, mentioned in Section 2) for the four alloys help to estimate the solubility limit of the corresponding matrix (cf. Table 2), which could be useful for further composition optimization. Microstructural in-depth characterization of the G-phase by HR-SEM,

TEM and APT proved that introduction of the G-phase into the Fe-20Cr-3Ni-1Mn-3Si ferritic alloy system by utilizing the Group IV and V elements was feasible. The so-called “Flexible” GTable phase may satisfy the multi-demands of alloying design principle for different fields of application. For example, Ta may be favored in creepresistant steels for high temperature application since it is not only the G-phase former for precipitation hardening (in this work), but also a very low-diffusion coefficient element (high melting point, 3017 °C) and thus beneficial for creep resistance of steels [43,44] and Co-based superalloys [45,46]. The high temperature deformation experiments outlined in Section 3.1 are still in progress.

For visual illustration of this compound, two representative phase diagrams (Fe-Zr-Si/Ni-Ti-Si [47,48]) are displayed in Fig. 6. The Febased G-phase usually appears as a linear compound (cf. Fig. 6a), while Ni-/Co-based G-phases present a stoichiometric compound (Fig. 6b). These two known characteristics were combined and plotted in the schematic diagram in Fig. 6c. It should be noticed that the different variants have different particle chemistry, which may provide some insight into particle chemistry evolution with the help of APT technology.

4.2. First-principles calculation

The ternary G-phases in Table 4 are thermodynamically favored based on experimental phase diagram determination. However, it was hard to distinguish and judge the relative stability of the different alloy systems. To overcome this problem, first principles calculations were utilized to quantitatively estimate their relative stabilities. The formation energies of the intermetallic compound structure, Ni16M6Si7 (M: transitional elements), were calculated according to the following equation:

$$EG_{\_formation} = (E_{Ni64M54Si50} - 64E_{Ni} - 54E_{M} - 50E_{Si})/168 \quad (2)$$

where $E_{Ni64M54Si50}$ is the total energy of the $Ni_{64}M_{54}Si_{50}$ supercells and ENi, EM and ESi are the chemical potentials of Ni, M and Si in dilute bcc Fe solid solution. Fig. 7 presents the calculated formation energies with a series of possible alloying elements occupying the M site. Several reported data ($Ni_{16}M_6Si_7$ (M=Zr, Hf, Mn and Ti)) - consistent with our present work - were plotted in addition. Obviously the formation entropy of the G-phase is lowest (−0.75 to −0.8 eV/atom, the most negative) in the IVB group (Hf, Zr, Sc and Ti) and increases step by step from the VB to the VIB group. This trend is consistent with previous experimental data and partly explains why no VIB-group G-phases exist. It is very likely that these VIB group G-phases are relatively instable when compared with potential competing phases (like Laves phase, Fe_2M) and thus cannot be observed in the experimental alloys.

4.3. Thermodynamic prediction

The stability of the G-phase in multicomponent ferritic alloy systems is discussed based on thermodynamic calculations. It should be noted that thermodynamic data were available for only three types (Ti-, Nb-, Zr-type) of G-phase in the present TCFE-7 database (Version 3.1). Therefore, Ti-, Nb-, Zr-type G-phase alloy systems are discussed in the following section. Because the effects of single Ni-, Si-, and Ti-alloying on G-phase precipitation was addressed in our previous work [26], two novel alloying philosophies (3Ni+3Si+2X and 5Ni+5Si+1.5X) were introduced to study the collective effect of combined alloying (X represents the alloying elements Ti, Zr and Nb). The (3Ni+3Si+2X) group was considered as “Low-G-High-L” (meaning: “low G-phase amount - high Laves phase amount”) type while the (5Ni+5Si+1.5X) was considered as “High-G-Low-L” one. The two calculated property diagrams are given in Fig. 8. Fig. 8a displays the simplified phase diagrams of the (3Ni+3Si+2X) group, Fig.

8b the diagrams of the (5Ni +5Si+1.5X) group. Note that only the main precipitates (G-phase and Laves phase) were considered, while other minor phases (like MC and M23C6 carbides) were ignored for simplicity. Comparing the two diagrams it becomes obvious, that the weight fraction of the Laves phase (all threes, Fe_2Ti, Fe_2Zr and Fe_2Nb) decreases remarkably when the alloying contents of Ti, Zr and Nb are diminished. In addition increasing the (Ni+Si)-level increases the temperature stability of G-phase from ~600–800 °C (3Ni+3Si) to ~900–1100 °C (5Ni+5Si). It seems that the G-phase weight fraction increases significantly in the XD-Ti alloy, but decreases slightly in the XD-Nb and XD-Zr alloys, demonstrating complex effects of the alloying elements on the G-phase in multi-component systems.

For comparison, the experimental data obtained by SEM, TEM and APT characterization were plotted in Fig. 8a. The experimental data of the XD-Ti sample range higher than the calculated curve, what may suggest that the temperature stability of the G-phase is underestimated in the present database version. A phase fraction v.s. temperature curve of the XD-Ta G-phase (dashed curve) was fitted to the experimental data points. The obtained thermodynamic data can be used for further thermodynamic optimization in the course of G-phase steel development.

5. Conclusions

The main focus of this contribution was on the demonstration of novel ferritic steels, hardened by nanoscale G-phase precipitates. With the help of thermodynamic and first principle calculations, the relative stabilities of varying G-phase types present in ternary and multicomponent alloy systems were systematically analyzed and a new 20Cr ferritic steel family was proposed. The following conclusions can be drawn from the presented research:

1. The mechanical properties of the four G-phase steels showed a significant precipitate hardening effect with the strongest age hardening at 560 °C in case of the Ti-type G-phase (~620 HV), followed by the Nb-type (~410 HV) and the Ta-type G-phases (~390 HV) and the Zr-type G-phase (~305 HV). The 660 °C compression experiments demonstrated that the studied G-phase steels offer low quasi steady-state deformation rates combating the reported FBB8 and commercial ferritic-martensitic steels like T/P92. Standard creep experiments have to be executed to confirm the promising properties derived from the compression experiments presented in this study.

2. The microstructures of the four trial alloys presented different Gphase distributions. The addition of 2 wt% of Ti may be sufficient to form G-phase precipitates, but has to considered to be excessive already in case of Ta-, Nb- and Zr-added steels, in which the Laves phase occurs at grain boundaries. The role of the GB Laves phase has to be studied in future research.

3. TEM observation revealed the microstructures of the four G-phase precipitate types. All have a cube-cube orientation relationship to the ferritic matrix in the intermediate temperature range from 560° to 860°C. The mean particle diameters in the four alloys were: Titype (less than 5 nm)< Zr-type (~5.5 nm) ≈ Nb-type (~6.5 nm)<Ta-type (~25 nm).

4. APT analysis of the strongest steel (XD-Ti) uncovered that the Titype G-phase precipitates have a spherical morphology with small mean radii of 1.6 ± 0.5 nm and a high number density of 6.05×10^{23} m^{-3}, which accounts for the good performance in mechanical tests.

5. By combining microstructural analyses, thermodynamic and first principle calculations, it was demonstrated how to introduce Gphase precipitates into a Fe-20Cr-3Ni-3Si ferritic alloy system by the addition of Nb, Ti, Ta and Zr. Based on the

presented results a new ferritic steel family, hardened by intermetallic compound G-phase precipitates, for high temperature application is proposed. Further alloy optimization towards higher temperature-stability and volume percentage of G-phase precipitates is in progress.

Acknowledgments

This work was financially supported by the National Key R&D Program of China (Grant No. 2017YFB0702901), the Ministry of Science and Technology of China (Grant No. 2014DFA53040) and the National Natural Science Foundation of China (Grant No. 51471138). Atom probe tomography research was conducted at the Inter-University 3D Atom Probe Tomography Unit of City University of Hong Kong, which is supported by the CityU grant 9360161 and CRF grant C1027- 14E. Z.B. Jiao would like to acknowledge the Open Fund of 2017-ZD01 from SKLAMM-USTB. M.J. Yang would like to acknowledge the China Scholarship Council (for 1 year's study abroad at Jülich GmbH, Institute for Energy and Climate Research, Microstructure and Properties of Materials (IEK-2)). We gratefully acknowledge the support of the Institute of Ferrous Metallurgy (IEHK) for providing the high purity raw metals. Also we gratefully acknowledge the support of C. Thomas (PGI- 5) in alloy preparation, B. Werner and V. Gutzeit (IEK-2) in mechanical testing and metallographic preparation and E. Wessel (IEK-2) in SEM investigations.

Conflicts of interest

The authors declare they have no conflicts of interest.

References

[1] L. Tan, T.S. Byun, Y. Katoh, L.L. Snead, Acta Mater. 71 (2014) 11–19.

[2] L. Tan, Y. Katoh, L.L. Snead, J. Nucl. Mater. 445 (2014) 104–110.
[3] Z. Teng, C. Liu, G. Ghosh, P. Liaw, M. Fine, Intermetallics 18 (2010) 1437–1443.
[4] Z. Teng, M.K. Miller, G. Ghosh, C.T. Liu, S. Huang, K.F. Russell, M.E. Fine, P.K. Liaw, Scr. Mater. 63 (2010) 61–64.
[5] Z. Teng, C.T. Liu, M.K. Miller, G. Ghosh, E.A. Kenik, S. Huang, P.K. Liaw, Mater. Sci. Eng.: A 541 (2012) 22–27.
[6] Z. Teng, F. Zhang, M. Miller, C.T. Liu, S. Huang, Y. Chou, R. Tien, Y. Chang, P. Liaw, Intermetallics 29 (2012) 110–115.
[7] K. Li, B. Yu, R. Misra, G. Han, S. Liu, C. Shang, Mater. Sci. Eng.: A (2018).
[8] H.K. Rafi, D. Pal, N. Patil, T.L. Starr, B.E. Stucker, J. Mater. Eng. Perform. 23 (2014) 4421–4428.
[9] I. Gutiérrez-Urrutia, D. Raabe, Mater. Sci. Technol. 30 (2014) 1099–1104.
[10] K. Choi, C.-H. Seo, H. Lee, S. Kim, J.H. Kwak, K.G. Chin, K.-T. Park, N.J. Kim, Scr. Mater. 63 (2010) 1028–1031.
[11] N. Kamikawa, Y. Abe, G. Miyamoto, Y. Funakawa, T. Furuhara, ISIJ Int. 54 (2014) 212–221.
[12] S.-I. Baik, M.J. Rawlings, D.C. Dunand, Acta Mater. 144 (2018) 707–715.
[13] Z. Sun, G. Song, J. Ilavsky, G. Ghosh, P.K. Liaw, Sci. Rep. 5 (2015) 16081.
[14] G. Song, Z. Sun, L. Li, X. Xu, M. Rawlings, C.H. Liebscher, B. Clausen, J. Poplawsky, D.N. Leonard, S. Huang, Sci. Rep. 5 (2015) 16327.
[15] Z. Sun, G. Song, J. Ilavsky, P.K. Liaw, Mater. Res. Lett. 3 (2015) 128–134.
[16] N.Q. Vo, C.H. Liebscher, M.J. Rawlings, M. Asta, D.C. Dunand, Acta Mater. 71 (2014) 89–99.
[17] G. Song, Z. Sun, J.D. Poplawsky, Y. Gao, P.K. Liaw, Acta Mater. 127 (2017) 1–16.
[18] S. Jiang, H. Wang, Y. Wu, X. Liu, H. Chen, M. Yao, B. Gault, D. Ponge, D. Raabe, A. Hirata, Nature 544 (2017) 460.
[19] S. Shu, B.D. Wirth, P.B. Wells, D.D. Morgan, G.R. Odette, Acta Mater. (2017).
[20] B. Chen, W. Wang, H. Xie, R. Ge, Z. Zhang, Z. Li, X. Zhou, B. Zhou, J. Microsc. 262 (2016) 123–127.
[21] H. Nakamichi, K. Yamada, K. Sato, J. Microsc. 242 (2011) 55–61.
[22] L. Feng, B. Zhou, J. Peng, J. Wang, Acta Metall. Sin. (Engl. Lett.) 26 (2013) 707–712.
[23] G. Frommeyer, U. Brüx, Steel Res. Int. 77 (2006) 627–633.
[24] G.R. Odette, G.E. Lucas, JOM-US 53 (2001) 18–22.
[25] D.M. Knowles, C.W. Thomas, D.J. Keen, Q.Z. Chen, Int. J. Press. Vessels Pip. 81 (2004) 499–506.
[26] M. Yang, J. Zhu, C. Wu, S. Yang, Z. Shi, C. Wang, X. Liu, Mater. Sci. Eng.: A (2018).
[27] M. Yang, C. Wang, S. Yang, Z. Shi, X. Liu, Mater. Lett. 209 (2017) 134–137.
[28] S. Brett, B. Kuhn, J. Rantala, C. Hyde, Mater. Adv. Power Eng. (2014).
[29] S. Li, Y. Wang, X. Wang, F. Xue, J. Nucl. Mater. 452 (2014) 382–388.
[30] Y. Matsukawa, T. Takeuchi, Y. Kakubo, T. Suzudo, H. Watanabe, H. Abe, T. Toyama, Y. Nagai, Acta Mater. 116 (2016) 104–113.
[31] C. Pareige, J. Emo, S. Saillet, C. Domain, P. Pareige, J. Nucl. Mater. 465 (2015) 383–389.
[32] G. Song, Z. Sun, L. Li, X. Xu, M. Rawlings, C.H. Liebscher, B. Clausen, J. Poplawsky, D.N. Leonard, S. Huang, Z. Teng, C.T. Liu, M.D. Asta, Y. Gao, D.C.

Dunand, G. Ghosh, M. Chen, M.E. Fine, P.K. Liaw, Sci. Rep. 5 (2015) 16327.
[33] G. Dimmler, P. Weinert, H. Cerjak, Int. J. Press. Vessels Pip. 85 (2008) 55–62.
[34] S. Tjong, J. Zhang, Scr. Metall. Et. Mater 30 (1994).
[35] Y. Zhao, H. Yao, X. Song, J. Jia, Z. Xiang, Met. Mater. Int. 24 (2018) 51–59.
[36] N.Q. Vo, C.H. Liebscher, M.J.S. Rawlings, M. Asta, D.C. Dunand, Acta Mater. 71 (2014) 89–99.
[37] J. Lopez Barrilao, B. Kuhn, E. Wessel, M. Talík, Mater. Sci. Technol. 33 (2017) 1056–1064.
[38] B. Kuhn, M. Talik, L. Niewolak, J. Zurek, H. Hattendorf, P.J. Ennis, W.J. Quadakkers, T. Beck, L. Singheiser, Mater. Sci. Eng.: A 594 (2014) 372–380.
[39] M. Takeyama, I. Tarigan, N. Takata, M. Ueda, Proceedings of the 3rd International ECCC Conference, Rome, Italy, May 5-7, 2014.
[40] S.W. Chen, C. Zhang, Z.X. Xia, H. Ishikawa, Z.G. Yang, Mater. Sci. Eng.: A 616 (2014) 183–188.
[41] W. Sun, R. Marceau, M. Styles, D. Barbier, C. Hutchinson, Acta Mater. 130 (2017) 28–46.
[42] J. Bentley, M. Miller, S. Brenner, J. Spitznagel, Proc. -Annu. Meet., Electron Microsc. Soc. Am. 43 (1985).
[43] H.K. Kim, J.W. Lee, J. Moon, C.H. Lee, H.U. Hong, J. Nucl. Mater. (2018).
[44] Y. Chun, S. Kang, S. Noh, T. Kim, D. Lee, S. Cho, Y. Jeong, J. Nucl. Mater. 455 (2014) 212–216.
[45] I. Povstugar, P.-P. Choi, S. Neumeier, A. Bauer, C.H. Zenk, M. Göken, D. Raabe, Acta Mater. 78 (2014) 78–85.
[46] B. Wang, J. Zhang, T. Huang, H. Su, Z. Li, W. Yang, L. Liu, H. Fu, Mater. Sci. Technol. 33 (2017) 377–380.
[47] L. Nathalie, M. Materials Science International Team, MSI, Materials Science International Services GmbH, Stuttgart.
[48] C.P. Wang, Y. Hu, S.Y. Yang, Y. Lu, Q.W. Jiang, X.J. Liu, J. Phase Equilib. Diffus. 34 (2013) 277–288.
[49] D. King, P. Burr, S. Middleburgh, T. Whiting, M. Burke, M. Wenman, J. Nucl. Mater. 505 (2018) 1–6.
[50] A. Grytsiv, X.-Q. Chen, P. Rogl, R. Podloucky, H. Schmidt, G. Giester, V. Pomjakushin, J. Solid State Chem. 180 (2007) 733–741.

Table 1 Nominal chemical composition of the studied trial steels (wt%).

Alloy No.	Cr	Mn	Ni	Si	X	Fe
XD-Ti	20	1	3	3	2Ti	Bal.
XD-Nb	20	1	3	3	2Nb	Bal.
XD-Ta	20	1	3	3	2Ta	Bal.
XD-Zr	20	1	3	3	2Zr	Bal.

[1]X means the G-phase forming elements include Ti, Nb, Ta and Zr, respectively.

Table 2 EDS analyses of the ferritic matrix and grain boundary phase in these aged specimens.

Alloy No.		Compositions by EDS (at%)				
		Cr	Ni	Mn	Si	X=
XD-Ti	Matrix	21.7±0.1	2.9±0.1	1.0 ± 0.1	5.3±0.1	1.9±0.0
XD-Nb	Matrix	21.0±0.3	2.9±0.1	1.0±0.05	5.0±0.0	0.8±0.1
	Laves-C14	11.4±0.2	2.5±0.1	0.6±0.1	11.8±0.1	24.7±0.1
XD-Ta	Matrix	21.0±0.2	2.8±0.2	1.0±0.1	5.5±0.1	0.4±0.1
	Laves-C14	/	/	/	/	/
XD-Zr	Matrix	22.6±0.2	2.4±0.1	0.9±0.2	5.0±0.1	0.1±0.0
	Laves-C15	7.0±0.5	7.8±0.4	0.5±0.0	14.5±0.6	20.7±0.1
	Laves-C36?	15.3±0.2	5.4±0.2	0.8±0.0	9.3±0.1	8.2±0.1

/ means it is too small to be detected by EDS.

X means the alloying elements, Ti, Nb, Ta and Zr, respectively.

Table 3 The average compositions of G-phase particle in the 500 °C / 5 h aged XD-Ti specimen.

Alloy		Composition (at%)				
		Cr	Ni	Mn	Si	X=
XD-Ti	Matrix Precipitates	19.72±0.30 4.34±2.12	2.13±0.15 39.63±3.75	0.63±0.07 0.37±0.36	4.97±0.19 25.62±5.22	0.16±0.05 14.15±4.14

Table 4 Occurrence of G-phase ($A_{16}M_6Si_7$) in ternary transition alloy systems.

A Transition Element ↓	← Transition Element M →											
	Group IV (4e/a)			Group V (5e/a)			Group VI (6e/a)			Group VII (7e/a)		
	Ti	Zr	Hf	V	Nb	Ta	Cr	Mo	W	Mn	Tc	Re
Fe(8e/a)	X	G	G	X	G	G	X	X	X	X	X	X
Co(9e/a)	G	G	G	X	G	G	X	X	X	X	X	X
Ni(10e/a)	G	G	G	G	G	G	G	X	X	G	X	X

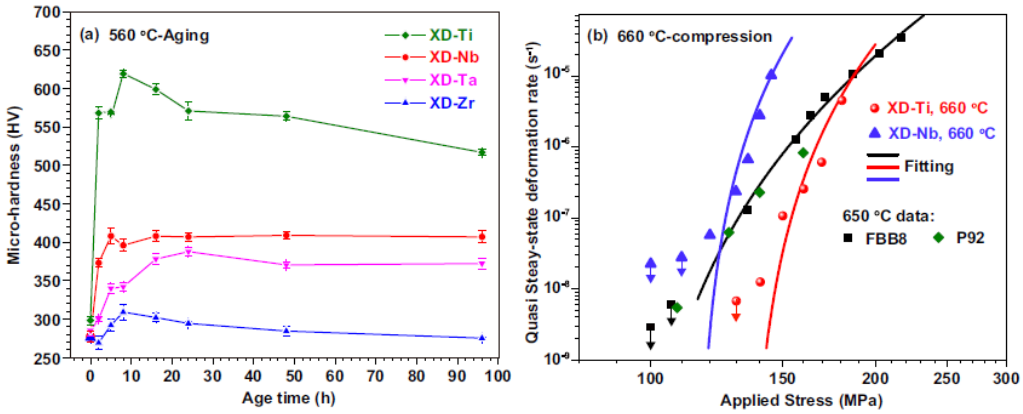

Fig. 1. Mechanical properties of the trial steels: (a) microhardness as a function of aging time at 560 °C (b) double logarithmic plot of quasi steady-state strain rate of compression vs. applied stress at 660 °C for XD-Ti (red) and XD-Nb alloys (purple). FBB8 and P92 data were obtained from Refs. [32,33]. Data with a downward arrow indicates upper bound values (discernible deformation rate not achieved).

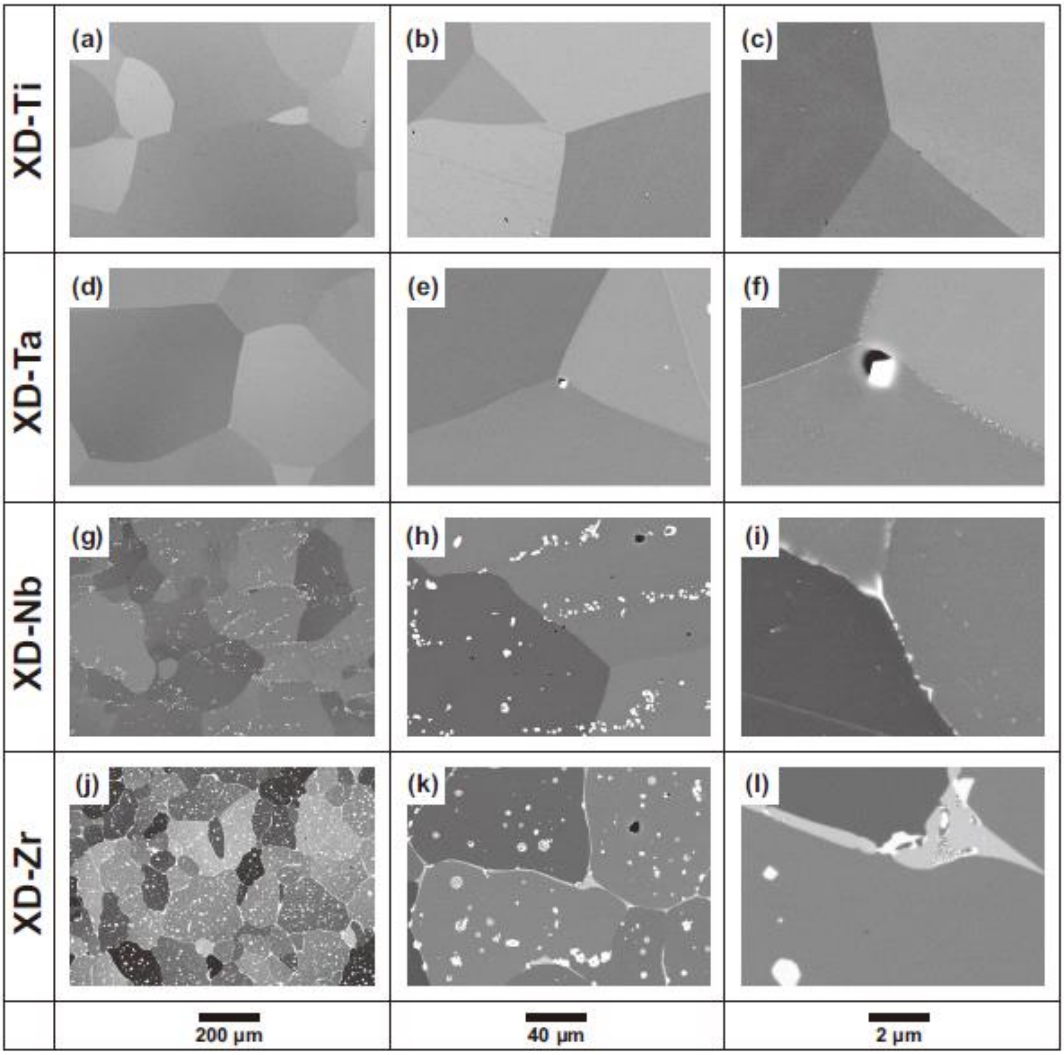

Fig. 2. SEM micrographs of various magnifications depicting the grain interior and grain boundary microstructures of the studied alloys after 560 °C / 8 h aging: (a), (b) and (c) were taken from XD-Ti, (d), (e) and (f) from XD-Ta, (g), (h) and (i) from XD-Nb, (j), (k) and (l) from XD-Zr.

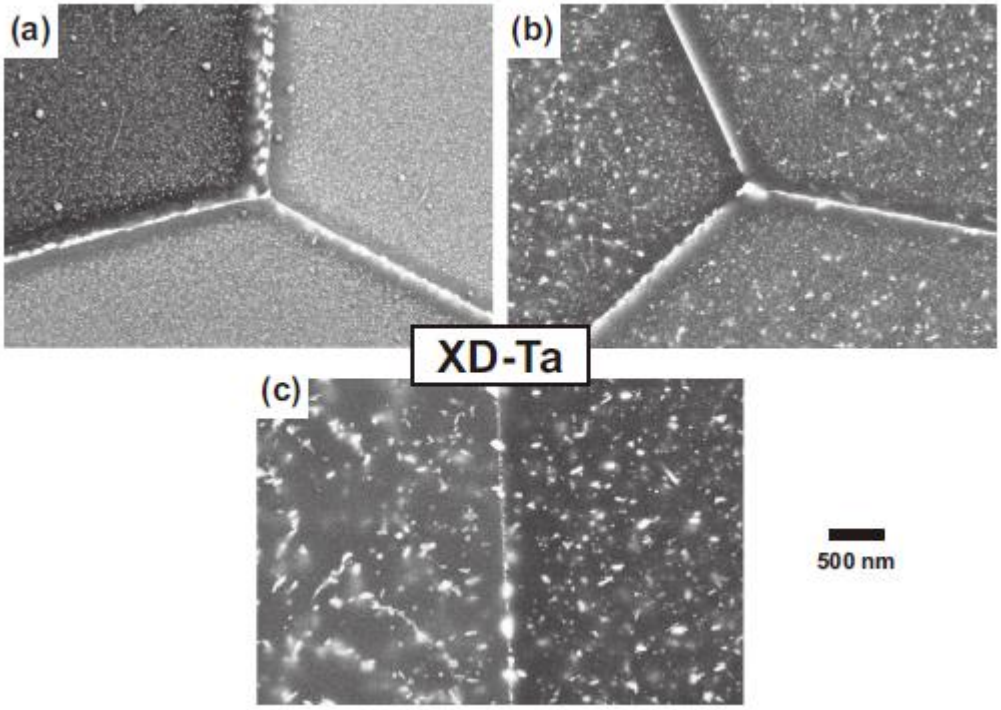

Fig. 3. High resolution SEM micrographs taken from the XD-Ta alloy showing nanoscale G-phase: (a) 660 °C ageing for 15 min, (b) 760 °C ageing for 15 min, (c) 860 °C ageing for 15 min.

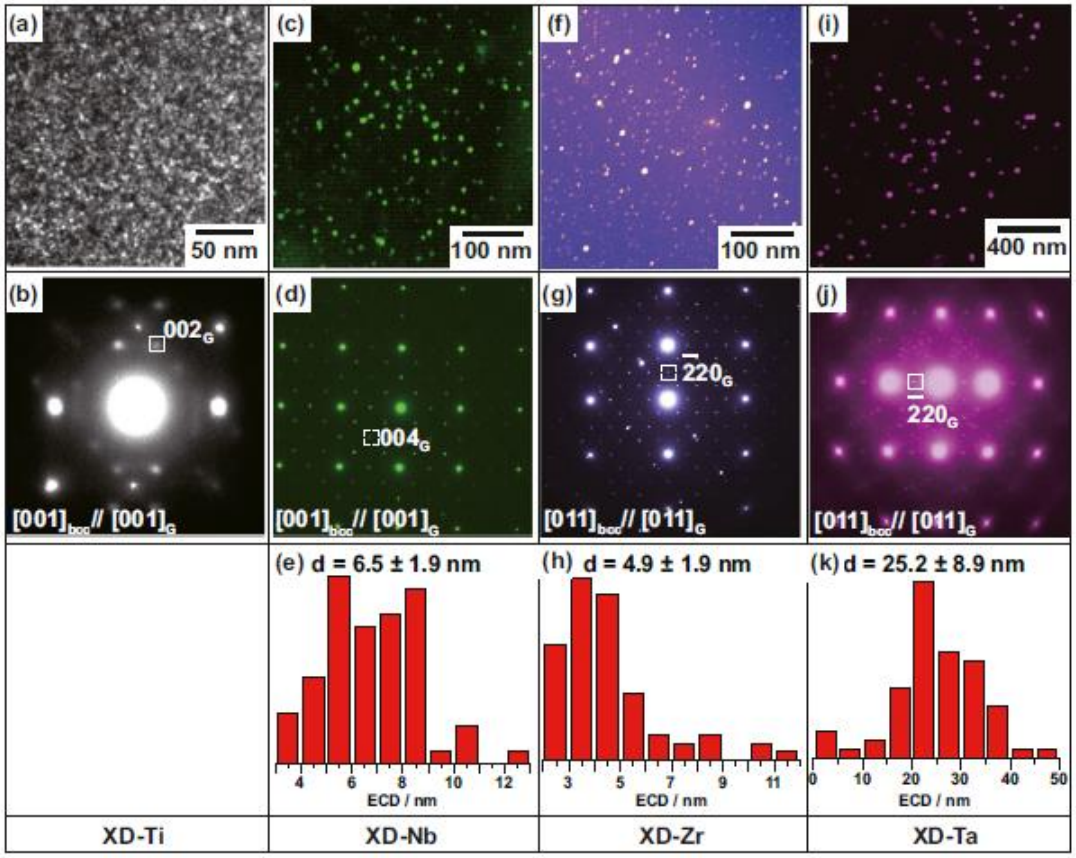

Fig. 4. TEM analysis of the aged specimens: Dark fields images (a), (c), (f), (i), which were taken from the 002_G, 004_G, -220_G, -220_G spots; corresponding diffraction patterns taken from the 560 °C / 8 h aged XD-Ti, 660 °C / 8 h aged XD-Nb, 660 °C / 8 h aged XD-Zr and 760 °C / 8 h aged XD-Ta (b), (d), (g), (j) and corresponding statistic particle distributions (e), (h) and (k). Note that the ECD in (e) to (k) means the equivalent circular diameter of these fine precipitate particles. More than 90 particles for each specimen were used for statistical analysis.

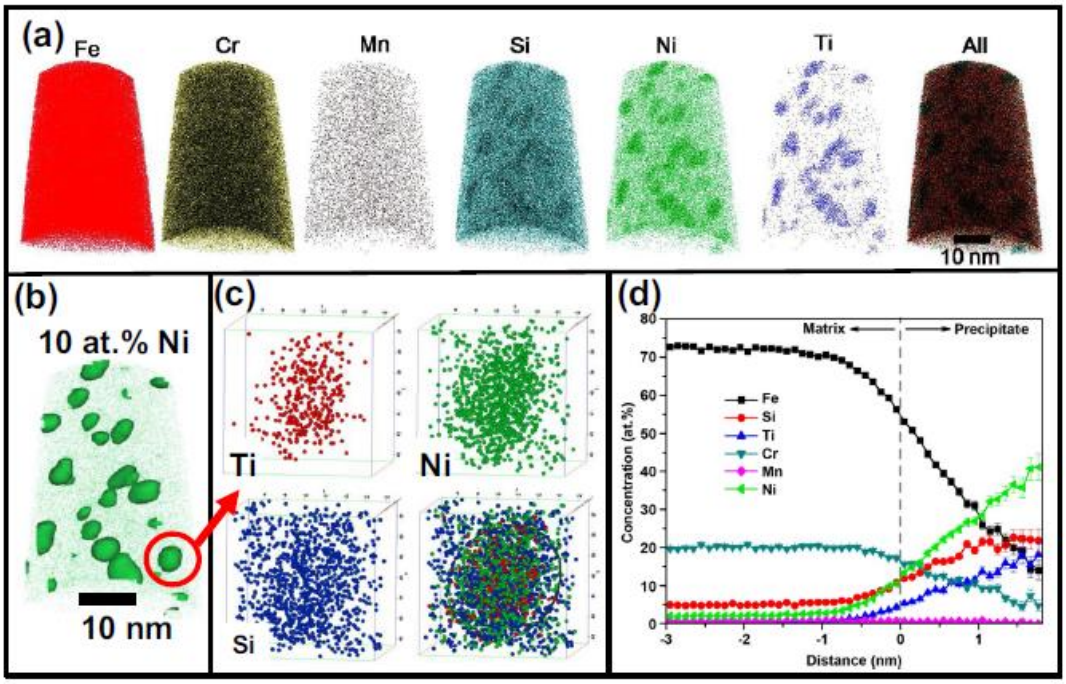

Fig. 5. APT characterization of the G-phase particles in the XD-Ti alloy after aging at 560 °C / 5 h: (a) elemental Fe, Cr, Mn, Si, Ni and Ti atom maps; (b) 10 at% Ni isoconcentration surface of G-phase; (c) selected high-resolution atom maps of an ultrafine G-phase particle; (d) Proximity histograms for Fe, Si, Ti, Cr, Mn and Ni for the G-phase precipitate. The reconstruction volume is ~35 nm×35 nm×55 nm and contains ~2 millions of ions.

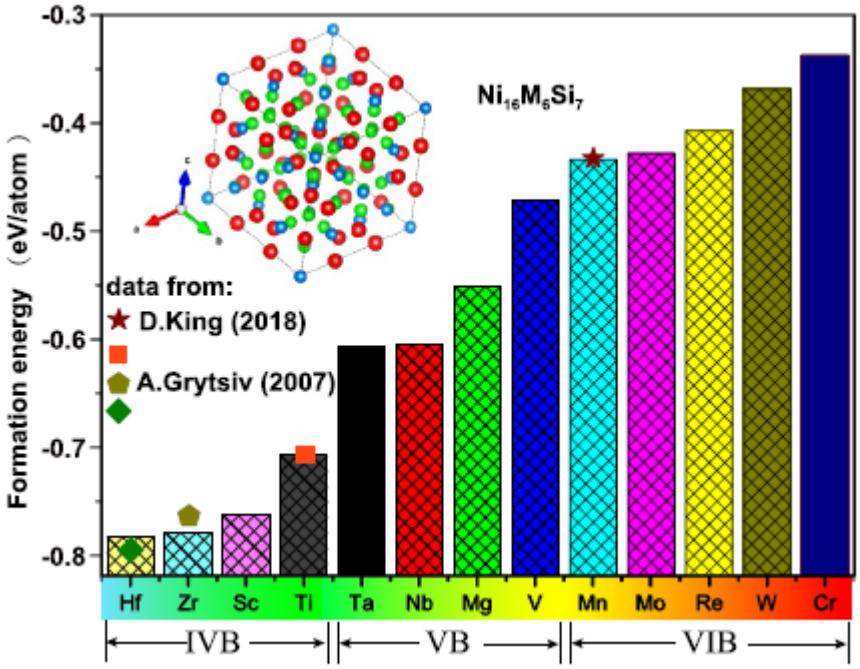

Fig. 7. The calculated formation enthalpies of the Ni16M6Si7 structure (Gphase) using the first principle method. Several reported data from Refs. [49,50] are plotted for comparison.

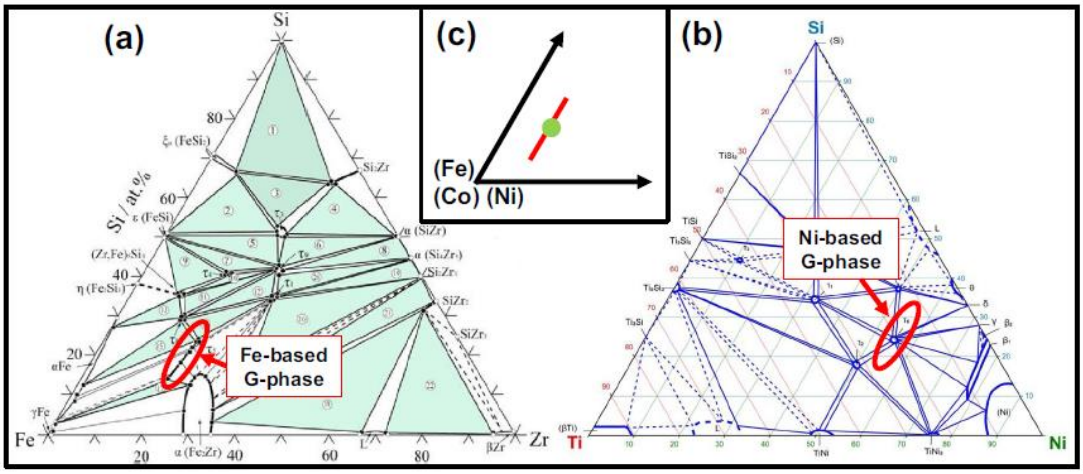

Fig. 6. Fig. 6. Representative phase diagrams with stable ternary G-phase: (a) Fe-based G-phase with a linear solubility [48]; (b) Ni-based G-phase in a stoichiometric ratio [47]; (c) schematic sketch map for two G-phase variants.

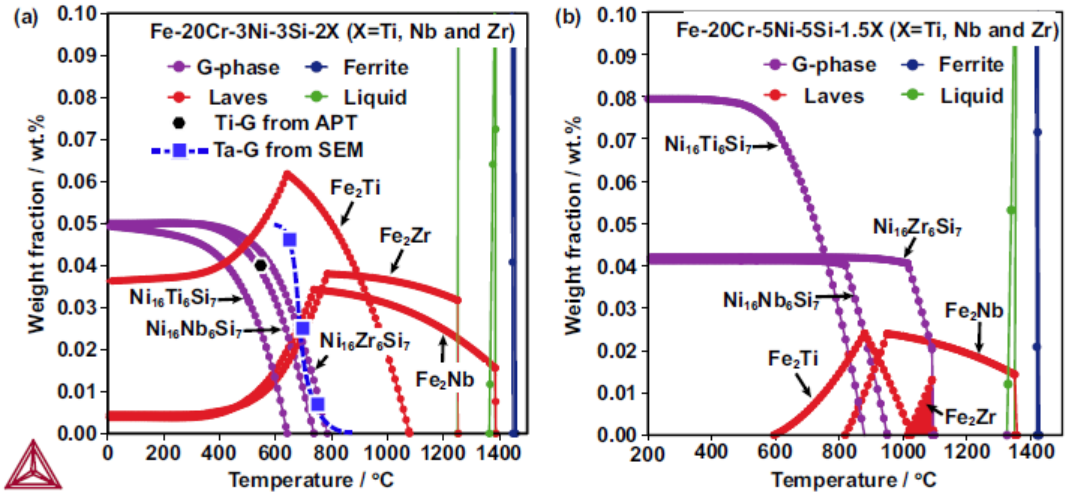

Fig. 8. Thermodynamic predictions in Fe-20Cr-X multicomponent alloy systems: (a) Fe-20Cr-3Ni-3Si-2X; (b) Fe-20Cr-5Ni-5Si-1.5X (X=Ti, Nb and Zr). Experimental verification data from SEM and APT plotted for comparison.